Journal of Water Process Engineering 54 (2023) 103972

Contents lists available at ScienceDirect

Journal of Water Process Engineering

journal homepage: www.elsevier.com/locate/jwpe

Constructing $BiOBr/TiO_2$ heterostructure nanotubes for enhanced adsorption/photocatalytic performance

Sheng-Zhe Zhao [a], Yun Lu [b], Ran Lu [a], Yong-Da Hu [b], Raul D. Rodriguez [c], Jin-Ju Chen [a,*]

[a] School of Materials and Energy, University of Electronic Science and Technology of China, Chengdu 610054, PR China
[b] School of Integrated Circuit Science and Engineering, University of Electronic Science and Technology of China, Chengdu 610054, PR China
[c] Tomsk Polytechnic University, 30 Lenin Ave, 634050 Tomsk, Russia

ARTICLE INFO

Keywords:
Electrospinning
Dual-function
Adsorption
Photocatalytic
Nanotubes

ABSTRACT

The fabrication of heterostructure materials with the synergy of adsorption and photocatalysis is an effective strategy to promote the removal of organic pollutants. In this work, $BiOBr/TiO_2$ nanotubes were successfully obtained to enhance the removal of organic pollutants from water via the synergy of adsorption and photocatalysis. The TiO_2 nanotubes were prepared using waste foam as the primary raw material by impregnation calcination, and BiOBr nanosheets were grown on their surface by a simple solvothermal method. The $BiOBr/TiO_2$ nanotubes have significantly enhanced separation efficiency of photo-generated carriers, synergistic adsorption, and photocatalytic decomposition compared with pure TiO_2 nanotubes. The enhanced activity is mainly attributed to the growth of BiOBr nanosheets leading to a substantial increase of the specific surface area and the internal electric field between the heterojunction of $BiOBr/TiO_2$. In addition, possible degradation pathways for organic pollutants are proposed based on trapping experiments, electron spin resonance spectrometer, and density functional theory calculations. Our work provides a promising strategy for combining the advantages of adsorption and photocatalytic technologies for environmental remediation, and we anticipate it will be of significant interest to researchers in environmental science, materials science, and chemical engineering.

1. Introduction

In recent years, antibiotics have been crucial in preserving human health. However, their excessive use also has several negative effects, including upsetting the ecological balance, endangering human health, and gravely disrupting the ecosystem [1–4]. Tetracycline hydrochloride (TCH), which is made from tetracycline and hydrochloric acid, has a noticeably increased water solubility [5]. As a refractory antibiotic agent, it might be stable in a water environment for an extended period of time [6–9]. However, conventional wastewater treatment methods, such as adsorption, precipitation, and biological treatment are difficult to achieve satisfactory processing efficiency, and the released effluent still threatens aquatic life and human health [10–13]. Generally speaking, adsorption is a cost-effective method of treating sewage [14,15]. However, the adsorption process does not eliminate environmental pollutants, which merely moves them from one phase to another, frequently resulting in secondary contamination [16,17]. Photocatalysis is regarded as a promising advanced oxidation processes (AOPs) for the oxidation or even mineralization of organic pollutants due to its high efficiency, low secondary pollution, ease of use, and low cost of treatment [18–20]. Titanium dioxide (TiO_2) has received much long-term attention in the process of degrading water contaminants [21–24]. However, due to its high rate of photogenerated charge recombination, it is difficult to employ sunlight to effectively destroy contaminants in industry [25–27]. In addition, the TiO_2 photocatalyst can only be stimulated by ultraviolet (UV) light because of the broad band gap energy ($E_g = 3.2$ eV), which accounts for only about 5 % of the solar energy [28–30]. Therefore, developing innovative techniques to produce TiO_2 with high solar usage and charge separation efficiency is crucial [31–33].

Bismuthyl bromide (BiOBr) is a type of layered oxide semiconductor containing tetragonal $[Bi_2O_2]^{2+}$ slabs sandwiched within double Br^- layers, which has been extensively researched for its excellent chemical stability, narrow band gap ($E_g = 2.69$ eV), and excellent photocatalytic activity [34,35]. Recent research works investigated the construction of the heterojunction structure of BiOBr and TiO_2 to enhance

* Corresponding author.
E-mail address: jinjuchen@uestc.edu.cn (J.-J. Chen).

https://doi.org/10.1016/j.jwpe.2023.103972
Received 9 April 2023; Received in revised form 16 June 2023; Accepted 23 June 2023
Available online 6 July 2023

photocatalytic performance, which could increase the visible light utilization efficiency and inhibit the recombination of photogenerated charge carriers [36,37]. For example, Yang et al. controlled the growth of BiOBr on TiO_2 nanorods, resulting that BiOBr/TiO_2 heterostructure displayed an enhanced photocatalytic performance in the decomposition of RhB under visible light [38]. Zhou et al. prepared BiOBr/TiO_2 heterojunction photocatalysts, which demonstrated excellent visible-light photocatalysis with 1.34 times and 12.63 times higher than that of bulk BiOBr and TiO_2, respectively [39]. However, developing low-cost, simple processes, and high-yield BiOBr/TiO_2 photocatalysts with higher photocatalytic activity is still challenging [40–42]. Compared to bulk semiconductor materials, controlling the nanoscale morphology has been employed to optimize the performance of photocatalysts [34,43]. Additionally, combining the adsorption and photocatalytic performance of the semiconductor heterostructure is also an effective approach for efficiently removing pollutants [44–46].

Herein, we constructed an adsorption-photocatalysis dual-functional photocatalyst by the BiOBr/TiO_2 heterojunction material. The uniform growth of BiOBr nanosheets on TiO_2 nanotubes not only maintains the morphology stability, but also reduce the recombination of charge carriers by the heterostructure. The TCH was used as a model pollutant to research the adsorption and catalytic performances of the BiOBr/TiO_2 nanotubes. Furthermore, the degradation mechanism of TCH was elucidated by free radical trapping experiments, electron spin resonance spectrometer (ESR), and density functional theory (DFT) calculations. This work will provide a simple and efficient method for manufacturing hollow heterojunction nanotubes, designing dual-functional adsorbent/photocatalysts and developing an excellent potential application for solving environmental problems.

2. Experimental section

2.1. Materials

Waste foam (the main component is polystyrene, PS) was collected from the outer package of Aladdin Industrial Corporation. Tetrabutyl titanate (TBOT, 97 %), bismuth nitrate pentahydrate ($Bi(NO_3)_3{\cdot}5H_2O$, 99 %), hexadecyl trimethyl ammonium bromide (CTAB, 99 %), tetracycline hydrochloride (TCH, 99 %), methyl orange (MO, 96 %), rhodamine B (RhB, 99 %), 1,4-benzoquinone (BQ, 99 %), disodium ethylenediaminetetraacetate (Na_2EDTA, 99 %), and tert-butyl alcohol (t-BuOH, 99 %) were purchased from Aladdin Industrial Corporation. *N*, *N*-dimethylformamide (DMF, 99 %), ethylene glycol (EG, 99 %), methylene blue (MB, 97 %) and absolute ethanol were obtained from Beijing chemical works. All chemicals used in experiments were of analytical grade and used without further purification.

2.2. Preparation of TiO_2 nanotubes

TiO_2 nanotubes were prepared by electrospinning combined with improved impregnation calcination. Firstly, 1.25 g PS was dissolved in 5 mL DMF to obtain the precursor solution. The PS nanofibers were manufactured using electrospinning equipment with a high voltage (16 kV) power supply. The ambient temperature was 25 °C and the ambient humidity was 40 %. The distance from the injector and acceptor was 14 cm, and the flow rate of the precursor solution was controlled at 0.5 mL/h to obtain the PS nanofibers membrane. Then the collected membrane was soaked in TBOT/ethanol (including 1 mL TBOT and 10 mL ethanol) solution for 1 min, and dried in an air oven at 60 °C for 2 h. Finally, the TBOT/PS nanofibers membrane was calcined at a heating rate of 2 °C /min to 550 °C and kept for 2 h, and let cool at room conditions after annealing to obtain TiO_2 nanotubes.

2.3. Preparation of BiOBr/TiO_2 heterostructures

0.4 g $Bi(NO_3)_3{\cdot}5H_2O$ and 0.45 g CTAB were firstly dissolved in 80 mL EG ethanol solution. Then, the above solution and a certain amount of TiO_2 nanotubes were transferred to a 100 mL Teflon-lined stainless-steel autoclave, sealed and heated for 4 h at 160 °C. Finally, the products were separated by centrifugation and washed with ethanol and deionized water three times (Scheme 1). The samples prepared with TiO_2 content of 150 mg, 100 mg, and 50 mg were named TB1, TB2, and TB3, respectively. As the control sample, pure BiOBr was synthesized with the same procedures without adding TiO_2 nanotubes.

The characterization instruments and parameters for the as-prepared photocatalysts are listed in the supplementary information.

2.4. Evaluation of adsorption activity

TCH has been widely used as a common antibiotic with low biodegradability in water. In this work, TCH (20 mg/L) was used as a simulated organic pollutant to evaluate the adsorption properties of the BiOBr/TiO_2 nanotubes. 40 mL TCH was put into a quartz tube, and 40 mg as-prepared catalysts were added into each quartz tube. The suspension was magnetically stirred in the dark, and 3 mL was extracted for centrifugation to measure the absorbance.

The detailed testing procedures for adsorption properties are presented in the supplementary information.

2.5. Evaluation of photocatalytic activity

The photocatalytic process of the as-prepared samples was evaluated by degradation of TCH. Firstly, 40 mg samples were mixed with 40 mL TCH (20 mg/L) in a quartz tube and stirred in the dark for 4 h to achieve the adsorption/desorption equilibrium. Then, the mixed dispersion was irradiated under a xenon light source (300 W); the distance between the tube and the xenon light was 10 cm. The content of TCH could be measured by UV–vis spectroscopy (Shimadzu, UV-2550) after being collected from the mixture (3 mL) and centrifuged at regular time intervals.

3. Results and discussion

Fig. 1a shows the scanning electron microscopy (SEM) of PS fibers with a diameter of 600–900 nm. After soaking and heating treatment, the hollow TiO_2 nanotubes with a diameter of about 800 nm were successfully fabricated, as shown in Fig. 1b-c. Compared with the pure TiO_2 nanotubes, the BiOBr/TiO_2 samples retain the nanotube morphology. Based on the observations from Fig. 1d-f, as the concentration of TiO_2 nanotubes decreases in the solvothermal reaction, there is a corresponding increase in the density of BiOBr nanosheets that cover the surface of the TiO_2 nanotubes. In Fig. 1e, the TiO_2 nanotubes marked as TB2 exhibit the most uniform and well-dispersed BiOBr nanosheets. This indicates that the quantity of the base material plays a crucial role in determining the morphology of the BiOBr nanosheets on the TiO_2 nanotubes. Fig. 1g shows the transmission electron microscopy (TEM) image of the TB2 nanotube, and a typical nanosheet structure of the BiOBr could be observed. In the HRTEM image of TB2 (Fig. 1h), the interplanar lattice spacing of 0.284 nm and 0.353 nm are found in the composite nanotubes, which corresponds to the (102) plane of BiOBr (JCPDS No. 09–0393) and the (101) plane of anatase TiO_2 (JCPDS No. 21–1272), respectively. It also confirms that BiOBr nanosheets grow on the TiO_2 nanotubes through a simple solvothermal reaction to form the heterostructure. Meanwhile, the energy dispersive X-ray (EDX) elemental mapping (Fig. 1i) corresponding to Fig. 1e further demonstrates that the BiOBr nanosheets are uniformly dispersed on the surface of TiO_2 nanotubes.

The X-ray diffraction (XRD) patterns of the BiOBr, TiO_2, and BiOBr/TiO_2 (TB2) nanotubes are shown in Fig. 2a. The diffraction peaks located at 25.34°, 37.83°, 48.13°, 55.13°, and 62.67° correspond to the (101), (004), (200), (211), and (204) lattice planes of the TiO_2 anatase phase (JCPDS No. 21–1272). Pure BiOBr exhibits peaks at 31.62° and 32.21°,

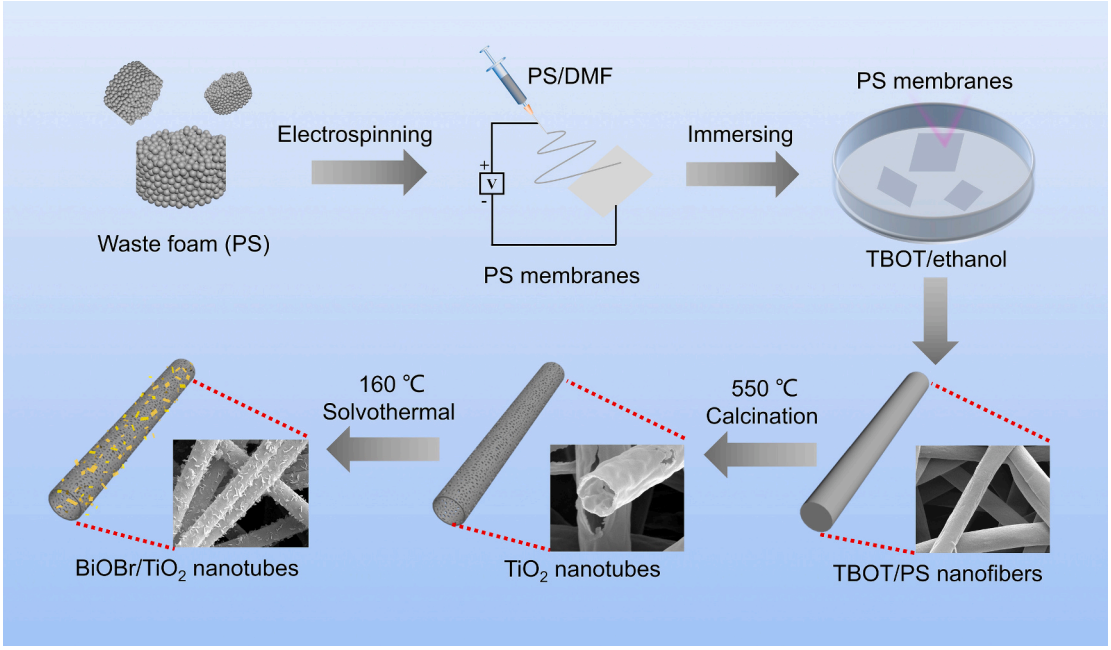

Scheme 1. Schematic for the fabrication of TiO_2 and BiOBr/TiO_2 nanotubes.

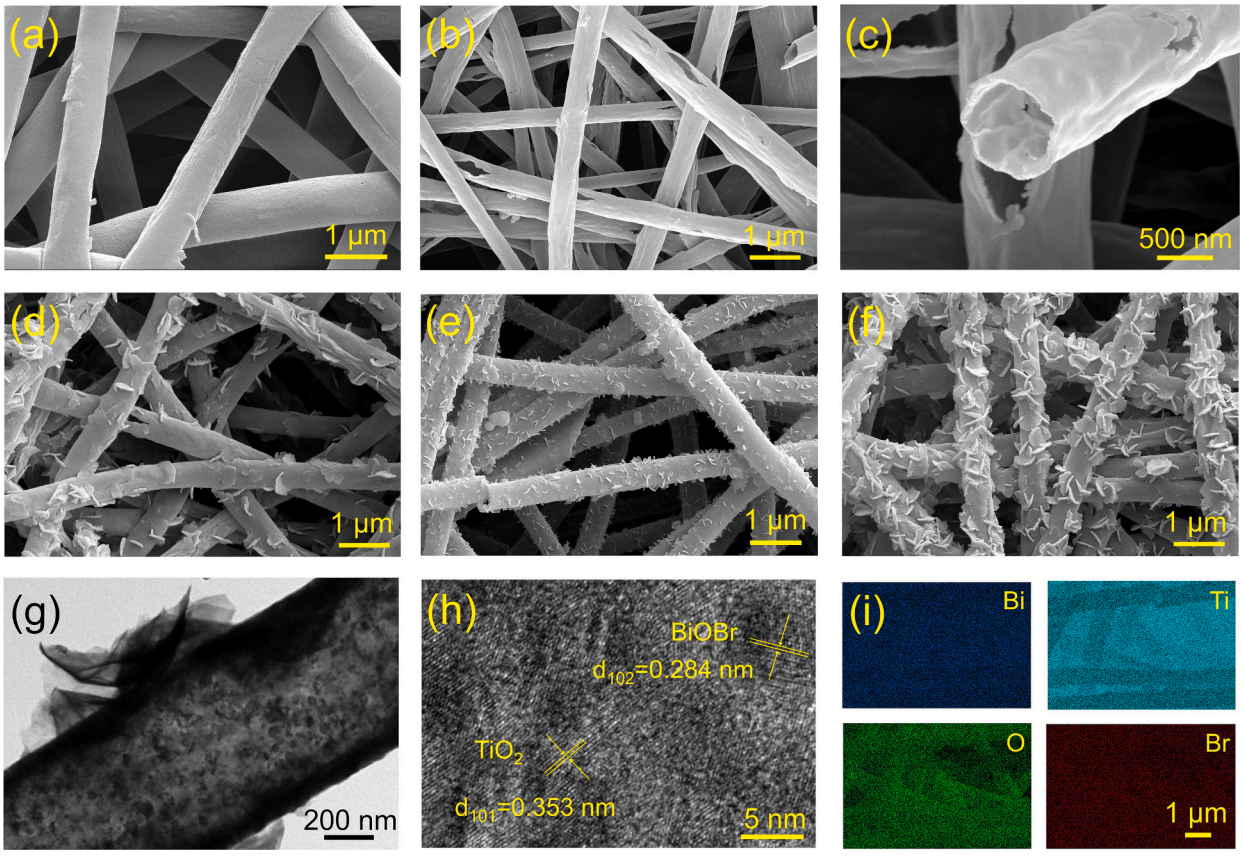

Fig. 1. SEM images of PS fibers (a), TiO_2 nanotubes (b, c), TB1 (d), TB2 (e), and TB3 (f). The TEM (g), HRTEM (h) and the EDX elemental mapping (i) of BiOBr/TiO_2 (TB2) nanotubes.

which can be attributed to the (102) and (110) lattice planes of the standard tetragonal phases BiOBr (JCPDS No. 09–0393). The BiOBr/TiO_2 nanotubes show the peaks of TiO_2 anatase and the BiOBr tetragonal phases. As shown in Fig. S1, the BiOBr diffraction peaks intensity strengthens as the relative concentration of Bi ions in the reaction increases. The sharp and intense diffraction peaks indicate that the obtained photocatalysts have good crystallinity and high purity.

Fig. 2b presents the X-ray photoelectron spectroscopy (XPS) results

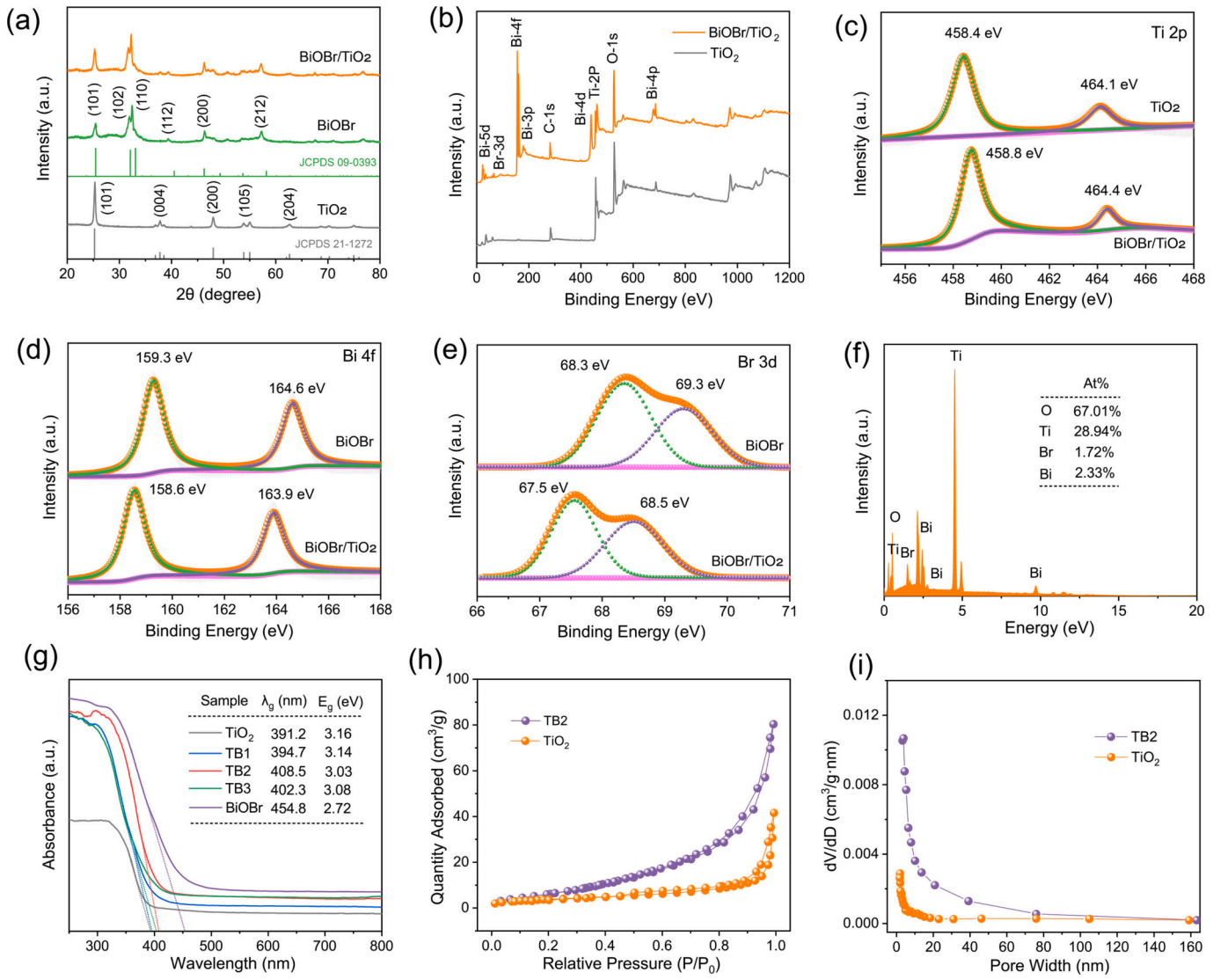

Fig. 2. XRD (a) and XPS patterns (b) of TiO_2 and $BiOBr/TiO_2$ (TB2) nanotubes. The high-resolution XPS patterns of Ti 2p (c), Bi 4f (d), Br 3d (e) in the TB2. EDX spectrum (f) of TB2 nanotubes. UV–vis diffuse reflectance spectra (g) and the deduced band gap energy of the samples. N_2 adsorption-desorption isotherms (h) and pore size distribution plots (i) of the TiO_2 and TB2.

of TiO_2 and $BiOBr/TiO_2$ (TB2) nanotubes. The survey XPS spectrum of TB2 clearly displays the peaks corresponding to Ti, O, Bi, and Br, confirming the presence of BiOBr and TiO_2. Moreover, the high-resolution XPS spectrum of Ti 2p for TB2 (Fig. 2c) reveals two peaks located at binding energies of 458.8 eV and 464.4 eV, corresponding to Ti $2p_{1/2}$ and Ti $2p_{3/2}$, respectively. The distance between the two peaks is 5.6 eV, demonstrating that Ti^{4+} is the main chemical state in TiO_2. Significantly, the binding energies of Ti for $BiOBr/TiO_2$ (TB2) nanotubes are 0.3–0.4 eV higher than that of TiO_2, which means that the electrons are transferred from TiO_2 to BiOBr when the $BiOBr/TiO_2$ heterojunction is formed. The high resolution XPS of Bi 4f (Fig. 2d) for TB2 shows two peaks at 158.6 and 163.9 eV. These peaks correspond to Bi $4f_{7/2}$ and Bi $4f_{5/2}$, which are the characteristic peaks of Bi^{3+} in BiOBr. The Br 3d spectrum (Fig. 2e) shows two peaks at 67.5 and 68.5 eV, corresponding to the Br $3d_{5/2}$ and Br $3d_{3/2}$ in TB2, respectively. The EDX spectrum of TC2 (Fig. 2f) demonstrates that Bi, O, Br, and Ti elements all exist in the composite nanotubes, and the corresponding atomic percentage are 2.33 %, 67.01 %, 1.72 % and 28.94 %, respectively. These collective XPS and EDS results indicate that the composite photocatalyst combines BiOBr and TiO_2 with an electron transfer process between these two components.

The UV–vis diffuse reflectance spectra (DRS) of the TiO_2, $BiOBr/TiO_2$, and BiOBr were recorded to analyze their light absorption properties. As shown in Fig. 2g, the pure TiO_2 nanotubes can only absorbs the UV light, the BiOBr and $BiOBr/TiO_2$ nanotubes can absorb UV light and an amount of visible light. The absorption intensity of $BiOBr/TiO_2$ nanotubes in the whole visible light range is significantly enhanced, which is due to the heterostructure between the BiOBr and TiO_2. The E_g values of the nanotubes are shown in the inset of Fig. 2g by the function [25]:

$$E_g = 1240/\lambda_g$$

The E_g values of TiO_2, TB1, TB2, TB3, and BiOBr were estimated to be 3.16, 3.14, 3.03, 3.08, and 2.72 eV, respectively. Clearly, the band gaps of $BiOBr/TiO_2$ nanotubes are smaller than that of pure TiO_2, which should be associated with $BiOBr/TiO_2$ heterostructure formation. Therefore, the $BiOBr/TiO_2$ nanotubes have an improved photocatalytic performance due to better visible light absorption.

Generally speaking, larger specific surface areas and pore volumes could provide more favorable conditions for photocatalytic processes. Therefore, the N_2 absorption-desorption isotherms of the as-prepared samples were obtained. As shown in Fig. 2h, the isotherms of TiO_2

and TB2 nanotubes all belong to type IV isotherm, indicating the existence of mesopores in the nanotubes. Meanwhile, the hysteresis loop of the TiO_2 and TB2 all belong to type H3, which implies the existence of narrow slit-shaped mesopores. Compared with pristine TiO_2 nanotubes, the TB2 nanotubes have a larger Brunauer-Emmett-Teller (BET) specific surface area from 14.3 m^2/g to 26.5 m^2/g as shown in Fig. 2h. The BiOBr/TiO_2 nanotubes possess an increased specific surface area, translating to more available surface reaction sites for the adsorption and decomposition of pollutant molecules. This characteristic ultimately leads to an improvement in photocatalytic activity.

The photocatalytic performance of the TiO_2 and BiOBr/TiO_2 nanotubes was evaluated by the degradation of TCH under xenon light irradiation, and the photocatalytic degradation efficiency of TCH was calculated by C_t/C_0 (C_t and C_0 correspond to the concentration of TCH at the time t, and the initial concentration of TCH, which conversion from the UV–vis spectroscopy by the Lambert-Beer law). In the dark, all samples reached the adsorption/equilibrium after two hours, and the pure TiO_2 nanotubes exhibited the lowest removal rate by adsorption (Fig. 3a). The adsorption rates (Fig. 3b) of TiO_2, TB1, TB2, and TB3 were estimated to be 24.4 %, 47.8 %, 55.7 %, and 64.1 %, which showed an upward trend with the increasing of BiOBr loading. After the adsorption/equilibrium under dark conditions, all samples were exposure to xenon light for 180 min. With the mass ratio of BiOBr increases, the photocatalytic activity of the as-prepared samples in the degradation of TCH first increased and then decreased (Fig. 3c), the TB2 reaching a maximum 88.1 %, which is higher than the pure TiO_2 (40.9 %), TB1 (76.9 %), and TB3 (82.3 %). The concentration of TCH does not change significantly without photocatalysts. In addition, the pseudo-first-order kinetic analysis is applied to compare the reaction kinetics of the degradation rate of TCH as follows [7]:

$$ln(C_0/C_t) = kt$$

where k is the pseudo-first-order rate constant, which could be used to measure the removal rate. As shown in Fig. 3d, the k values follow the order of TB2 (0.0074 min^{-1}) > TB3 (0.0039 min^{-1}) > TB1 (0.0047 min^{-1}) > TiO_2 (0.00128 min^{-1}). The TC2 nanotubes exhibit the highest photocatalytic activity, which is 5.8 times higher than that of pure TiO_2 nanotubes. The improved photocatalytic efficiency of BiOBr/TiO_2 nanotubes may be due to the following reasons. First, the high specific surface area increases the active site of the reaction. Second, the enhanced adsorption performance is more conducive to capturing pollutant molecules. Third, the heterostructure between the interface of BiOBr and TiO_2 provides more electron immigration pathways, promoting photogenerated electron-hole separation and transport.

The adsorption process has a significant effect on the removal of organic pollutants. Therefore, different types of adsorption experiments were performed under dark conditions to investigate the adsorption performance of BiOBr/TiO_2 nanotubes, as shown in Fig. 4. The adsorption curves (Fig. 4a) of TCH by TB2 was estimated from the Fig. 3a, and the corresponding pseudo-first and pseudo-second-order models of the TB2 are shown in Fig. 4b and c. These results show that the pseudo-first-order dynamics description (R^2 = 0.991) is more consistent with the experimental process than the pseudo-second-order (R^2 = 0.984). Therefore, the adsorption capacity of the composite nanotubes can be enhanced by an appropriate modification with BiOBr. To further explore the adsorption mechanism of BiOBr/TiO_2 nanotubes, the adsorption process of TCH in different initial concentrations by TB2 was studied (Fig. 4d), the data were analysed using the Langmuir (Fig. 4e) and the Freundlich (Fig. 4f) isotherm models. The result was better described by the Freundlich model based on its higher coefficient of determination (R^2 = 0.992), which indicated that the adsorption of TCH onto TB2 transpired via multilayer adsorption.

In general, the photocatalytic degradation process of the organic pollutants is mainly driven by different reactive oxygen species from the photocatalysts, such as holes (h^+), superoxide radical ($\bullet O_2^-$), and hydroxyl radical (•OH). To better identify the active species driving the photocatalytic process, trapping experiments were performed for TCH degradation with TB2 nanotubes with Na_2EDTA, BQ, and t-BuOH used as scavengers for h^+, $\bullet O_2^-$, and •OH, respectively. Generally speaking, the specific scavengers can react with reactive oxygen species faster than

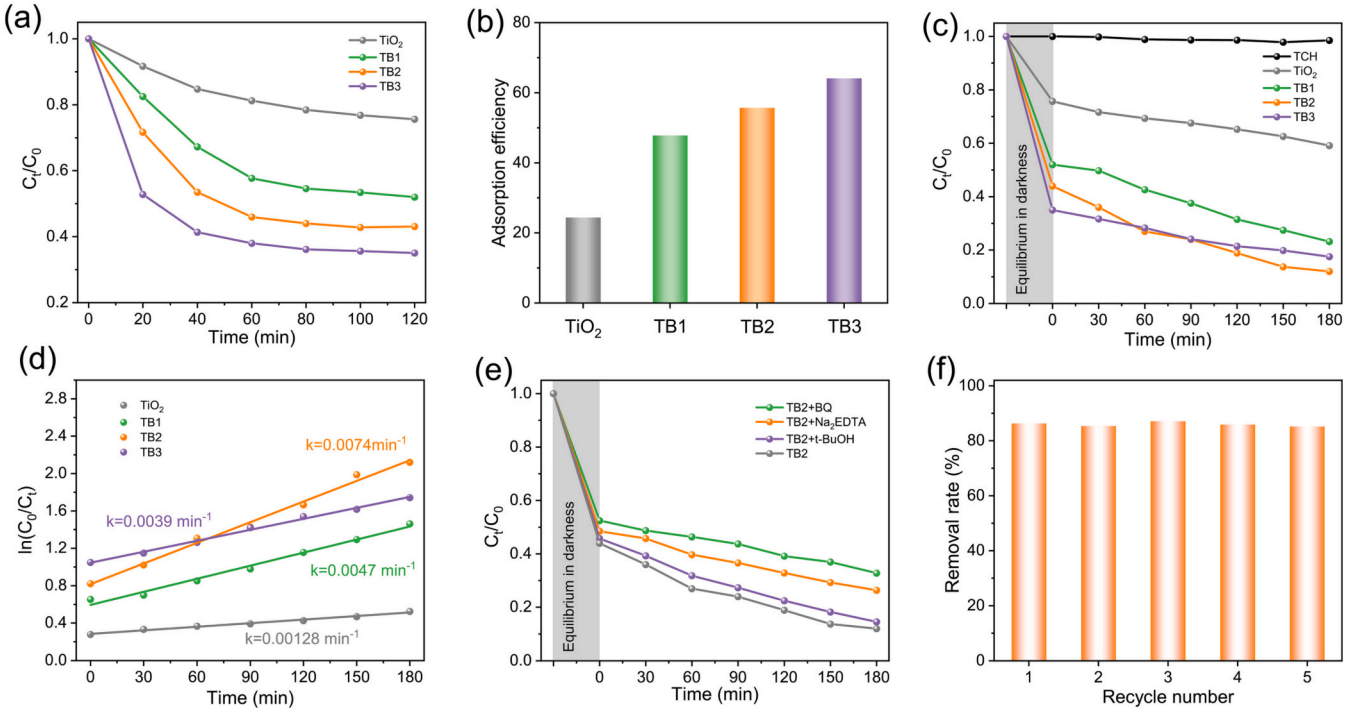

Fig. 3. The TCH adsorption curves (a) and adsorption rates (b) of the as-prepared samples in the darkness. The photocatalytic degradation of TCH (c) and the corresponding pseudo-first-order kinetic curves (d) of the as-prepared nanotubes under xenon light irradiation. The photocatalytic activity of TCH containing different scavengers (e) and the five recycling runs of TCH degradation over the TB2 (f).

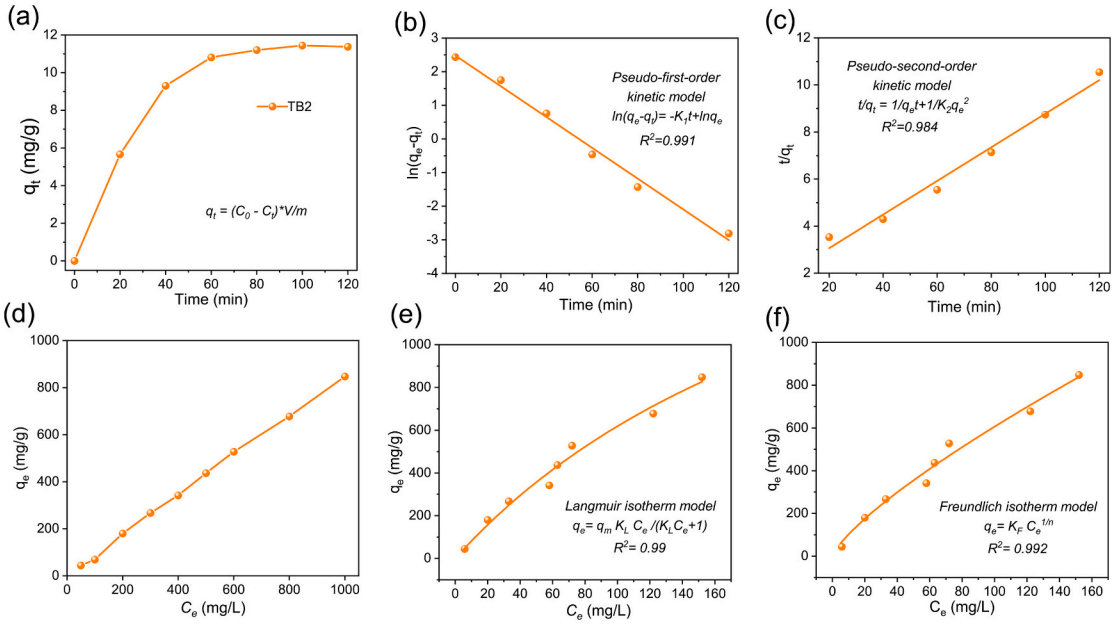

Fig. 4. The TCH adsorption curves (a), the pseudo first-order model (b) and pseudo second-order models for the TB2 (c). The TCH adsorption curves in different initial concentrations (d), the Langmuir (e) and Freundlich (f) isotherm models for the TB2.

organic pollutant molecules, resulting in the photodegradation rate decreased [5]. As shown in Fig. 3e, after adding BQ the photodegradation efficiency was significantly inhibited, which means the $\bullet O_2^-$ is the main active species in the process of TCH photodegradation. To further verify the active species from the trapping experiments, the ESR experiments were performed with 5,5-dimethyl-1-pyrroline N-oxide (DMPO) as the radical trapping agent. As shown in Fig. S2, no evident signal is observed in the dark, and show the obvious characteristic signal of $\bullet O_2^-$ under xenon lamp light condition, which means the $\bullet O_2^-$ is reactive oxygen species in this system [47,48]. Meanwhile, the photodegradation efficiency of the TB2 was not significantly reduced after five cycles as shown in Fig. 3f, indicating that it has excellent stability during the photocatalytic reaction. Besides, the XRD pattern exhibit no significant change after the cycles as well (Fig. S3).

Common dyes MB, MO, and RhB were used as simulated contaminants to further analyze the adsorption and degradation properties of $BiOBr/TiO_2$ (TB2) nanotubes, and the removal rates (Fig. 5a) of the pollutants are about 67.9 %, 88.8 %, 92.8 % and 86.3 % corresponding

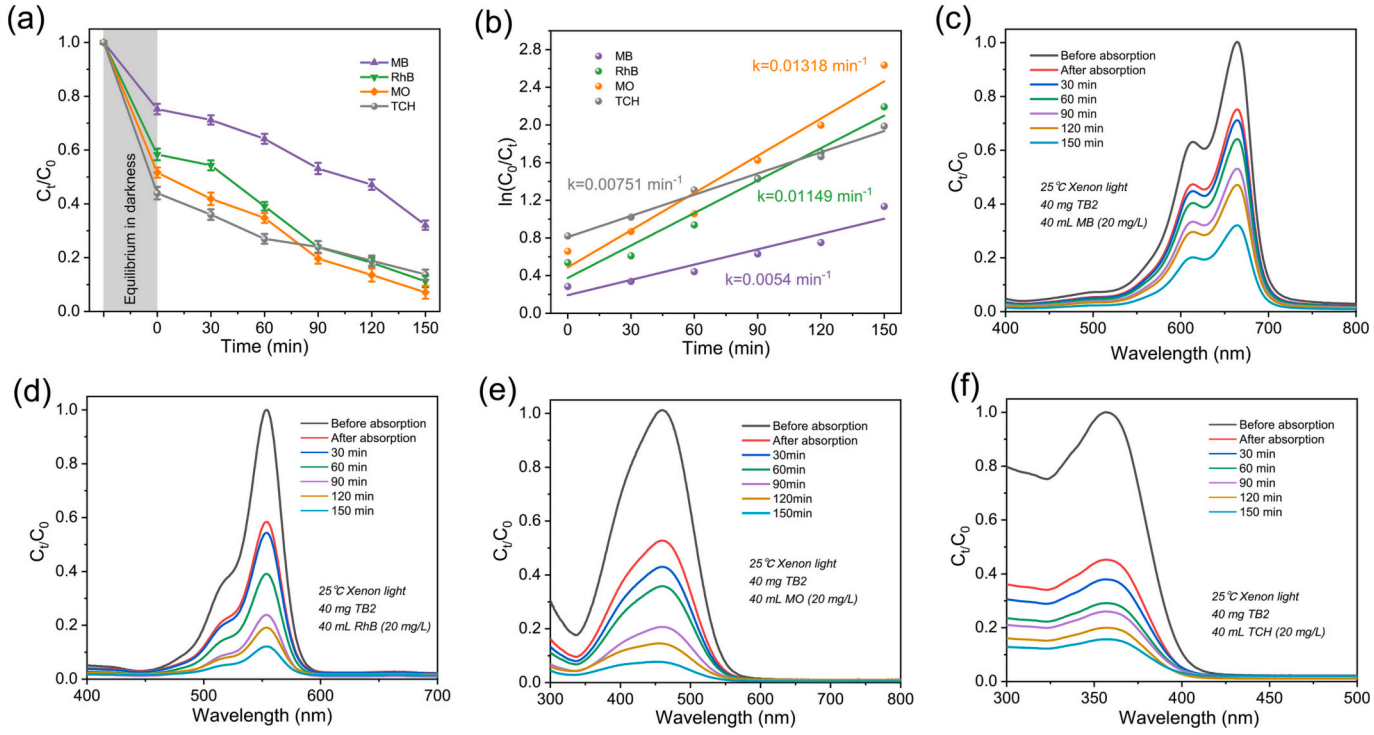

Fig. 5. The photocatalytic degradation of common organic pollutants (a), pseudo-first-order kinetic curves (b), and the corresponding UV–vis spectra of MB (c), RhB (d), MO (e) and TCH (f) over the TB2 nanotubes under xenon light irradiation.

to MB, RhB, MO and TCH by TB2, respectively. It is worth noting that the potential and relative molecular weight of the pollutants have great influence on the adsorption process. The organic pollutant molecule with negative potential (TCH, MO) showed stronger adsorption rate than that with positive potential (MB, RhB) by the TB2 nanotubes [20]. Based on our previous research, this phenomenon maybe caused by the $[Bi_2O_2]^{2+}$ slabs in the BiOBr/TiO_2 nanotubes, which with a high positive potential and causes the potential adsorption [7]. Fig. 5b shows the pseudo-first-order kinetic analysis corresponding to the Fig. 5a, and the k values of the different pollutants shown a similar order with the adsorption rates, which means the adsorption process can directly affect the subsequent photodegradation, and the faster adsorption is advantageous to the degradation process. Fig. 5c-f shows the UV–vis spectra of MB, RhB, MO, and TCH by TB2 corresponding to the Fig. 5a. The absorption peak of the pollutants showed a significant decrease without red or blue shift, indicating that the pollutants were directly decomposed without intermediate products.

Generally, the photocurrent intensities directly reflect the ability of photogenerated charge transfer and separation. The photocurrent response curves of the samples under a xenon lamp with 50 s on-off cycles are presented in Fig. 6a. The photocurrent intensities display sharp rises and drops in sync with the light source turned on and off. The TB2 nanotubes exhibit a photocurrent density response obviously higher than that of pure TiO_2 nanotubes, indicating that the BiOBr/TiO_2 heterostructure nanotubes could efficiently promote the separation and transfer of photogenerated carriers under the xenon lamp light illumination. It is worth noting that the back part of photocurrent intensities TB2 go up increased obviously than the pure TiO_2 nanotubes. This phenomenon may be caused by the unstable current of the xenon lamp source at startup, and the light response ability of the BiOBr/TiO2 nanotubes is stronger than the pure TiO_2 nanotubes, which leads to significant fluctuations.

The photoluminescence (PL) emission spectra of TiO_2 and BiOBr/TiO_2 nanotubes are exhibited in Fig. 6b. Significantly, compared with pristine TiO_2, the emission peak of BiOBr/TiO_2 nanotubes is significantly weaker. Because the PL spectra could be related to the separation efficiency of photogenerated electron/hole pairs, and a lower emission intensity means a higher separation efficiency. Therefore, the recombination rate of photogenerated electrons and holes in BiOBr/TiO_2 nanotubes is lower than in pristine TiO_2 nanotubes. These results suggest that BiOBr nanosheets formed on the interface of TiO_2 nanotubes could effectively promote the separation of photogenerated carrier and improve photocatalytic activity. Electrochemical impedance spectroscopy (EIS) curves of TiO_2 and TB2 nanotubes are shown in Fig. 6c. The radius of the TB2 nanotubes is much smaller than pure TiO_2, which means the charge transfer resistance in the BiOBr/TiO_2 nanotubes is lower than that of the pure TiO_2, facilitating separation and transfer of photogenerated carriers [49]. This phenomenon can be attributed to the heterojunction between BiOBr and TiO_2 that effectively hinders the recombination of photogenerated carriers.

For further exploring the photogenerated carrier transfer mechanism, the Mott-Schottky plots were measured to investigate the flat potential of TiO_2 and BiOBr nanotubes, as shown in Fig. 6d and e. The Mott-Schottky curves of the pure TiO_2 showing a positive slope indicate that the sample is an n-type semiconductor. Therefore, the conduction band (CB) positions can be estimated by the flat band potential, which is ascertained to be −0.71 V (vs. Ag/AgCl, pH = 7) for TiO_2 nanotubes based on the x-intercepts of Mott-Schottky curves [49]. Thus, the CB of TiO_2 is located at −0.51 eV (vs. NHE, pH = 0). According to the UV–vis DRS analysis of TiO_2 (3.16 eV) and the formula $E_g = E_{VB}\text{-}E_{CB}$, the valence band (VB) position of TiO_2 is calculated to be 2.65 eV (vs. NHE, pH = 0). Similarly, the CB and VB potentials of pure BiOBr are calculated to be 0.08 and 2.8 eV, respectively. Meanwhile, first-principles calculations of differential charge density (DFT) of BiOBr/TiO_2 heterojunction were carried out and the result is shown in Fig. 6f. The yellow and blue regions represent net electron accumulation and depletion, respectively. Distinctly, the electron accumulates in the BiOBr part and the holes accumulate in the interface between TiO_2 and BiOBr, which indicates that the BiOBr/TiO_2 belongs to heterojunction in agreement with Mott-Schottky and XPS analyses.

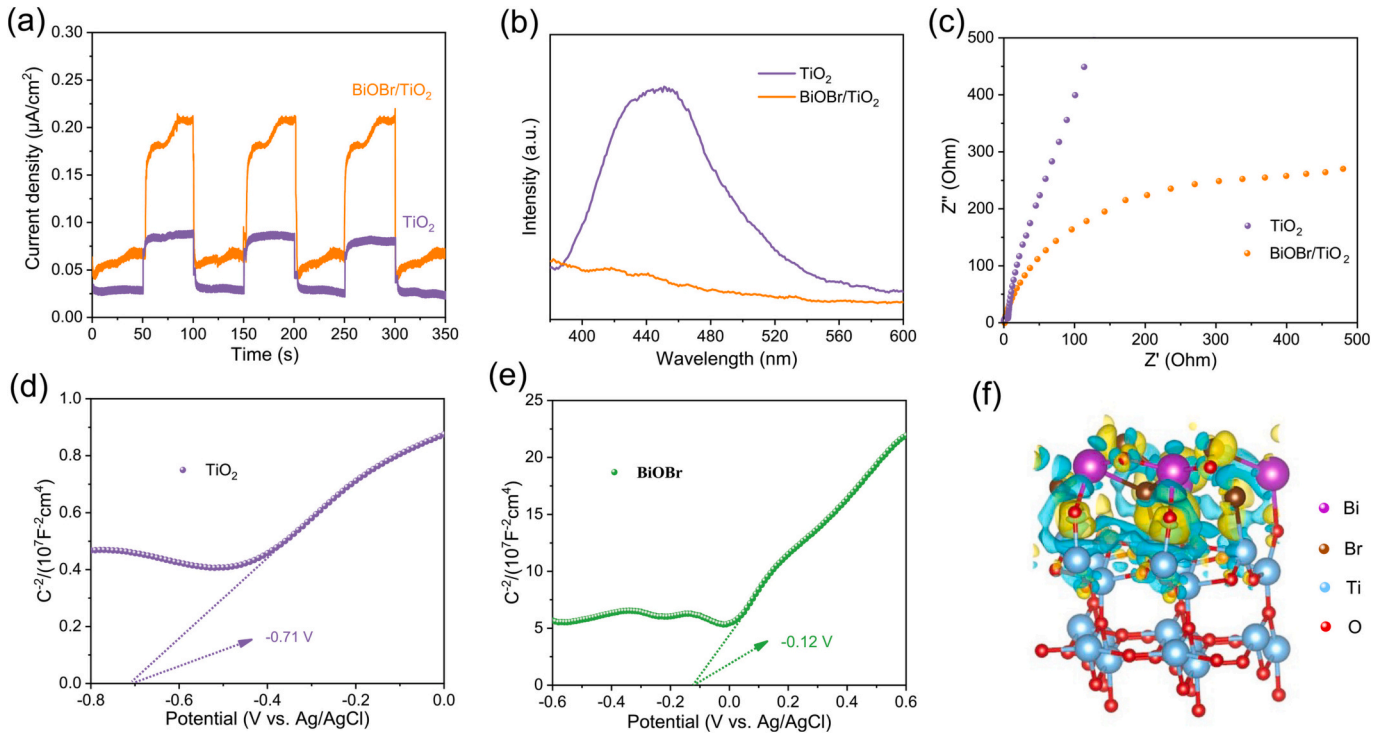

Fig. 6. The transient photocurrent response (a), PL spectra (b), and EIS (c) of TiO_2 and BiOBr/TiO_2 (TB2) nanotubes. The Mott-Schottky plots of TiO_2 (d) and BiOBr (e). The differential charge density (DFT) of BiOBr/TiO_2 (f).

Based on the results of trapping experiments, ESR, DFT calculations, and Mott-Schottky plots, a possible band energy diagram of BiOBr/TiO_2 *Z*-scheme heterojunction is displayed in Fig. 7, and a reasonable mechanism for the enhanced photoactivity of BiOBr/TiO_2 is proposed. The growth of BiOBr on the surface of TiO_2 leads to the transfer of electrons from TiO_2 to BiOBr to achieve Fermi energy level equilibrium, while holes diffuse from BiOBr to TiO_2 due to the difference in carrier density. This observation is consistent with the results obtained from DFT calculations [50]. Due to the charge redistribution between BiOBr and TiO_2, an internal electric field from TiO_2 to BiOBr is formed at the interface. Under xenon lamp irradiation, the photogenerated electrons in TiO_2 and BiOBr are excited to their CB, and leave holes on the VB of TiO_2 and BiOBr simultaneously. The built-in electric field promotes the transfer of photogenerated electrons from BiOBr to TiO_2 that combine with the photogenerated holes in TiO_2. Ultimately, the electrons in TiO_2 and the holes in BiOBr with strong redox ability remain spatially separated without recombination, contributing to enhanced photocatalytic performance.

4. Conclusion

In summary, BiOBr/TiO_2 nanotubes have been successfully synthesized by combining electrospinning, impregnation calcination and solvothermal method. Waste foam was used as raw material to save preparation costs. The BiOBr/TiO_2 nanotubes showed remarkable improvement in photo-generated carriers, synergistic adsorption, and photocatalytic decomposition for organic pollutants compared with pure TiO_2 nanotubes. The formation mechanism of BiOBr/TiO_2 nanotubes and the reason for enhanced photocatalytic performance were also elucidated. This research provides a new method for designing and preparing heterostructure nanotubes for inexpensive and efficient environmental remediation applications powered by sunlight.

Abbreviations

tetracycline hydrochloride TCH
electron spin resonance spectrometer ESR
advanced oxidation processes AOPs
titanium dioxide TiO_2
bismuthyl bromide BiOBr
ultraviolet UV
electron spin resonance spectrometer ESR
density functional theory DFT
polystyrene PS
tetrabutyl titanate TBOT
bismuth nitrate pentahydrate $Bi(NO_3)_3{\cdot}5H_2O$
hexadecyl trimethyl ammonium bromide CTAB
methyl orange MO
rhodamine B RhB
1,4-benzoquinone BQ
disodium ethylenediaminetetraacetate Na_2EDTA
tert-butyl alcohol t-BuOH
N, *N*-dimethylformamide DMF
ethylene glycol EG
methylene blue MB
X-ray powder diffraction XRD
scanning electron microscopy SEM
energy dispersive X-ray analysis EDX
transmission electron microscopy TEM
X-ray photoelectron spectroscopy XPS
diffuse reflectance spectra DRS
Brunauer-Emmett-Teller BET
holes h^+
superoxide radical $\bullet O_2^-$
hydroxyl radical $\bullet OH$
5,5-dimethyl-1-pyrroline N-oxide DMPO
photoluminescence spectra PL
electrochemical impedance spectroscopy EIS
conduction band CB
valence band VB

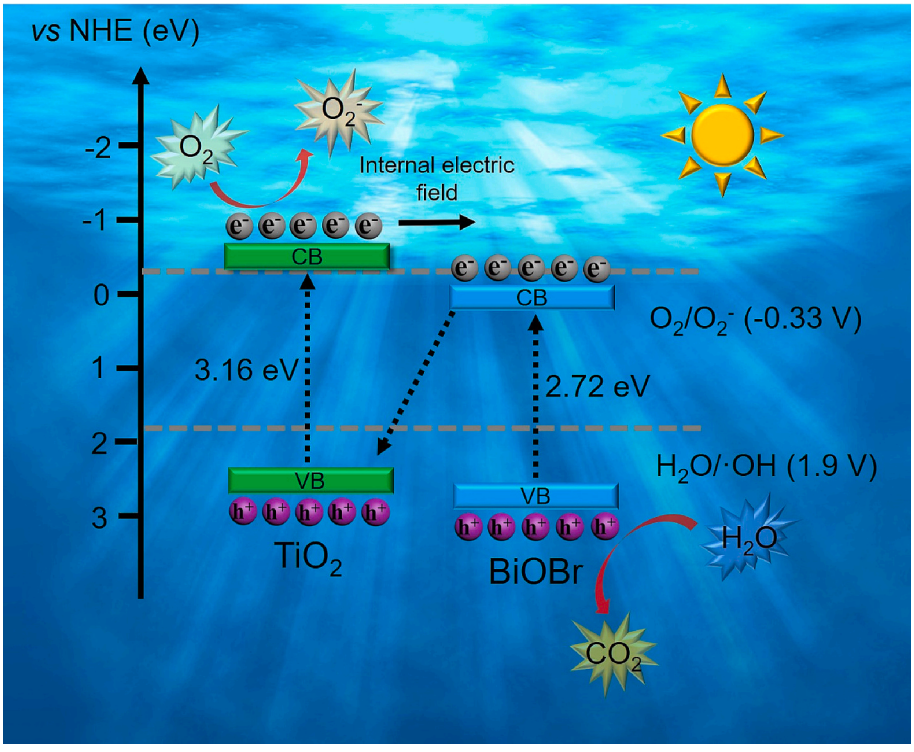

Fig. 7. Schematic representation of electron-hole separation and transportation in BiOBr/TiO_2 nanotubes under simulated solar light irradiation.

Declaration of competing interest

The authors declare that they have no known competing financial interests or personal relationships that could have appeared to influence the work reported in this paper.

Data availability

The data that has been used is confidential.

Acknowledgements

The work was supported by the Sichuan Science and Technology Program (grant No 2023YFG0215). RDR thanks support by RFBR and DFG, project number 21-53-12045.

Appendix A. Supplementary data

Supplementary data to this article can be found online at https://doi.org/10.1016/j.jwpe.2023.103972.

References

[1] Q. Chen, W. Yang, J. Zhu, L. Fu, D. Li, L. Zhou, Enhanced visible light photocatalytic activity of g-C_3N_4 decorated ZrO_{2-x} nanotubes heterostructure for degradation of tetracycline hydrochloride, J. Hazard. Mater. 384 (2020), 121275.
[2] X. Zhang, B. Xu, S. Wang, X. Li, C. Wang, Y. Xu, R. Zhou, Y. Yu, H. Zheng, P. Yu, Y. Sun, Carbon nitride nanotubes anchored with high-density CuN_x sites for efficient degradation of antibiotic contaminants under photo-Fenton process: performance and mechanism, Appl. Catal. B Environ. 306 (2022), 121119.
[3] D. Zhou, H. Luo, F. Zhang, J. Wu, J. Yang, H. Wang, Efficient photocatalytic degradation of the persistent PET fiber-based microplastics over Pt nanoparticles decorated N-doped TiO_2 nanoflowers, Adv. Fiber Mater. 4 (2022) 1094–1107.
[4] X. Li, T. Liu, Y. Zhang, J. Cai, M. He, M. Li, Z. Chen, L. Zhang, Growth of BiOBr/ZIF-67 nanocomposites on carbon fiber cloth as filter-membrane-shaped photocatalyst for degrading pollutants in flowing wastewater, Adv. Fiber Mater. 4 (2022) 1620–1631.
[5] J. Ni, W. Wang, D. Liu, Q. Zhu, J. Jia, J. Tian, Z. Li, X. Wang, Z. Xing, Oxygen vacancy-mediated sandwich-structural TiO_{2-x}/ultrathin g-C_3N_4/TiO_{2-x} direct Z-scheme heterojunction visible-light-driven photocatalyst for efficient removal of high toxic tetracycline antibiotics, J. Hazard. Mater. 408 (2021), 124432.
[6] X. Ma, Q. Chen, G. Liu, Y. Zhou, D. Ma, S. Xin, C. Yu, B. Zhang, Y. Xin, Construction of netlike 3D Z-scheme photoelectrodes with improved photocatalytic performance based on g-C_3N_4 nanosheets modified TiO_2 nanobelt-tubes, Chem. Eng. Sci. 226 (2020), 115844.
[7] S. Zhao, Y. Yang, R. Lu, Y. Wang, Y. Lu, R.D. Rodriguez, E. Sheremet, J. Chen, Enhanced selective adsorption and photocatalytic of ag/Bi_2O_3 heterostructures modified up-conversion nanoparticles, J. Environ. Chem. Eng. 10 (2022), 107107.
[8] Q. Wang, Z. Fang, W. Zhang, D. Zhang, High-efficiency g-C_3N_4 based photocatalysts for CO_2 reduction: modification methods, Adv. Fiber Mater. 4 (2022) 342–360.
[9] Y. Zhang, A. Sun, M. Xiong, D.K. Macharia, J. Liu, Z. Chen, M. Li, L. Zhang, TiO_2/BiOI p-n junction-decorated carbon fibers as weavable photocatalyst with UV–vis photoresponsive for efficiently degrading various pollutants, Chem. Eng. J. 415 (2021), 129019.
[10] S. You, Y. Hu, X. Liu, C. Wei, Synergetic removal of Pb(II) and dibutyl phthalate mixed pollutants on Bi_2O_3-TiO_2 composite photocatalyst under visible light, Appl. Catal. B Environ. 232 (2018) 288–298.
[11] Y. Liu, X. Wang, Q. Sun, M. Yuan, Z. Sun, S. Xia, J. Zhao, Enhanced visible light photo-Fenton-like degradation of tetracyclines by expanded perlite supported $FeMo_3O_x$/g-C_3N_4 floating Z-scheme catalyst, J. Hazard. Mater. 424 (2022), 127387.
[12] Y. Li, G. Wang, H. Zhang, W. Qian, D. Li, Z. Guo, R. Zhou, J. Xu, Hierarchical flower-like 0D/3D g-C_3N_4/TiO_2 S-scheme heterojunction with enhanced photocatalytic activity, Colloids Surf. A Physicochem. Eng. Asp. 646 (2022), 128942.
[13] H. Zhai, Z. Liu, L. Xu, T. Liu, Y. Fan, L. Jin, R. Dong, Y. Yi, Y. Li, Waste textile reutilization via a scalable dyeing technology: a strategy to enhance dyestuffs degradation efficiency, Adv. Fiber Mater. 4 (2022) 1595–1608.
[14] F. Dalanta, T.D. Kusworo, Synergistic adsorption and photocatalytic properties of AC/TiO_2/CeO_2 composite for phenol and ammonia–nitrogen compound degradations from petroleum refinery wastewater, Chem. Eng. J. 434 (2022), 134687.
[15] X. Lian, W. Xue, S. Dong, E. Liu, H. Li, K. Xu, Construction of S-scheme Bi_2WO_6/g-C_3N_4 heterostructure nanosheets with enhanced visible-light photocatalytic degradation for ammonium dinitramide, J. Hazard. Mater. 412 (2021), 125217.
[16] Z. Dai, Y. Zhen, Y. Sun, L. Li, D. Ding, $ZnFe_2O_4$/g-C_3N_4 S-scheme photocatalyst with enhanced adsorption and photocatalytic activity for uranium(VI) removal, Chem. Eng. J. 415 (2021), 129002.
[17] G.B. Vieira, H.J. José, M. Peterson, V.Z. Baldissarelli, P. Alvarez, R. de Fátima Peralta, Muniz Moreira, CeO_2/TiO_2 nanostructures enhance adsorption and photocatalytic degradation of organic compounds in aqueous suspension, J. Photochem. Photobiol. A Chem. 353 (2018) 325–336.
[18] H. Yan, R. Wang, R. Liu, T. Xu, J. Sun, L. Liu, J. Wang, Recyclable and reusable direct Z-scheme heterojunction CeO_2/TiO_2 nanotube arrays for photocatalytic water disinfection, Appl. Catal. B Environ. 291 (2021), 120096.
[19] Y. Geng, N. Li, J. Ma, Z. Sun, Preparation, characterization and photocatalytic properties of BiOBr/ZnO composites, J. Energy Chemistry 26 (2017) 416–421.
[20] Z. Cheng, S. Zhao, L. Han, A novel preparation method for ZnO/gamma-Al_2O_3 nanofibers with enhanced absorbability and improved photocatalytic water-treatment performance by Ag nanoparticles, Nanoscale 10 (2018) 6892–6899.
[21] J. Ma, C. Wang, H. He, Enhanced photocatalytic oxidation of NO over g-C_3N_4-TiO_2 under UV and visible light, Appl. Catal. B Environ. 184 (2016) 28–34.
[22] R. Hao, G. Wang, C. Jiang, H. Tang, Q. Xu, In situ hydrothermal synthesis of g-C_3N_4/TiO_2 heterojunction photocatalysts with high specific surface area for rhodamine B degradation, Appl. Surf. Sci. 411 (2017) 400–410.
[23] F.O. Esmaeili, M. Tasviri, N. Mohaghegh, A $Cd_xZn_{1-x}S$/TiO_2 nanotube array electrode for a highly sensitive and selective nonenzymatic photoelectrochemical glucose sensor, New J. Chem. 46 (2022) 9880–9888.
[24] M. Faraji, N. Mohaghegh, Ag/TiO_2-nanotube plates coated with reduced graphene oxide as photocatalysts, Surf. Coat. Technol. 288 (2016) 144–150.
[25] Z. Cheng, S. Zhao, Z. Han, Y. Zhang, X. Zhao, L. Kang, A novel preparation of Ag@TiO_2 tubes and their potent photocatalytic degradation efficiency, CrystEngComm 18 (2016) 8756–8761.
[26] X. Qian, M. Ren, D. Yue, Y. Zhu, Y. Han, Z. Bian, Y. Zhao, Mesoporous TiO_2 films coated on carbon foam based on waste polyurethane for enhanced photocatalytic oxidation of VOCs, Appl. Catal. B Environ. 212 (2017) 1–6.
[27] S. Ma, W. Song, B. Liu, W. Zhong, J. Deng, H. Zheng, J. Liu, X.-Q. Gong, Z. Zhao, Facet-dependent photocatalytic performance of TiO_2: a DFT study, Appl. Catal. B Environ. 198 (2016) 1–8.
[28] S. Zhao, Z. Cheng, L. Kang, Y. Zhang, X. Zhao, A novel preparation of porous spong-shaped Ag/ZnO heterostructures and their potent photocatalytic degradation efficiency, Mater. Lett. 182 (2016) 305–308.
[29] N. Mohaghegh, B. Eshaghi, E. Rahimi, M.R. Gholami, Ag_2CO_3 sensitized TiO_2 nanoparticles prepared in ionic liquid medium: a new Ag_2CO_3/TiO_2/RTIL heterostructure with highly efficient photocatalytic activity, J. Mol. Catal. A Chem. 406 (2015) 152–158.
[30] N. Mohaghegh, M. Endo-Kimura, K. Wang, Z. Wei, A. Hassani Najafabadi, F. Zehtabi, N. Hosseinzadeh Kouchehbaghi, S. Sharma, A. Markowska-Szczupak, E. Kowalska, Apatite-coated Ag/AgBr/TiO_2 nanocomposites: insights into the antimicrobial mechanism in the dark and under visible-light irradiation, Appl. Surf. Sci. 617 (2023), 156574.
[31] N. Mohaghegh, M. Faraji, F. Gobal, M.R. Gholami, Electrodeposited multi-walled carbon nanotubes on Ag-loaded TiO_2 nanotubes/Ti plates as a new photocatalyst for dye degradation, RSC Adv. 5 (2015) 44840–44846.
[32] Q. Wang, S. Zhu, S. Zhao, C. Li, R. Wang, D. Cao, G. Liu, Construction of Bi-assisted modified CdS/TiO_2 nanotube arrays with ternary S-scheme heterojunction for photocatalytic wastewater treatment and hydrogen production, Fuel 322 (2022), 124163.
[33] Q. Wang, Y. Zhao, Z. Zhang, S. Liao, Y. Deng, X. Wang, Q. Ye, K. Wang, Hydrothermal preparation of Sn_3O_4/TiO_2 nanotube arrays as effective photocatalysts for boosting photocatalytic dye degradation and hydrogen production, Ceram. Int. 49 (2023) 5977–5985.
[34] X. Sun, W. He, X. Hao, H. Ji, W. Liu, Z. Cai, Surface modification of BiOBr/TiO_2 by reduced AgBr for solar-driven PAHs degradation: mechanism insight and application assessment, J. Hazard. Mater. 412 (2021), 125221.
[35] K. Wang, Q. Wang, Y. Zhao, Z. Zhang, S. Liao, Y. Deng, X. Wang, Q. Ye, Hydrothermal synthesis of Z-scheme Bi_2WO_6/Bi_2MoO_6 heterojunctions for the enhanced photoelectrocatalytic performance of TiO_2 NTs: structure, activity and mechanism approach, Fuel 339 (2023), 126973.
[36] X. Liu, X. Duan, T. Bao, D. Hao, Z. Chen, W. Wei, D. Wang, S. Wang, B.J. Ni, High-performance photocatalytic decomposition of PFOA by BiOX/TiO_2 heterojunctions: self-induced inner electric fields and band alignment, J. Hazard. Mater. 430 (2022), 128195.
[37] Y. Jia, P. Liu, Q. Wang, Y. Wu, D. Cao, Q.A. Qiao, Construction of $Bi_{(2)}S_{(3)}$-BiOBr nanosheets on $TiO_{(2)}$ NTA as the effective photocatalysts: pollutant removal, photoelectric conversion and hydrogen generation, J. Colloid Interface Sci. 585 (2021) 459–469.
[38] C. Xue, T. Zhang, S. Ding, J. Wei, G. Yang, Anchoring tailored low-index faceted BiOBr nanoplates onto TiO_2 nanorods to enhance the stability and visible-light-driven catalytic activity, ACS Appl. Mater. Interfaces 9 (2017) 16091–16102.
[39] M. Zou, C. Tan, H. Yang, D. Kuang, Z. Nie, H. Zhou, Facile preparation of recyclable and flexible BiOBr@TiO_2/PU-SF composite porous membrane for efficient photocatalytic degradation of mineral flotation wastewater, J. Water Process Eng. 50 (2022).
[40] X. Wang, G. Xu, Y. Tu, D. Wu, A. Li, X. Xie, BiOBr/PBCD-B-D dual-function catalyst with oxygen vacancies for acid Orange 7 removal: evaluation of adsorption-photocatalysis performance and synergy mechanism, Chem. Eng. J. 411 (2021), 128456.
[41] M. Faraji, N. Mohaghegh, A. Abedini, Ternary composite of $TiO_{(2)}$ nanotubes/Ti plates modified by g-$C_{(3)}N_{(4)}$ and $SnO_{(2)}$ with enhanced photocatalytic activity for enhancing antibacterial and photocatalytic activity, J. Photochem. Photobiol. B 178 (2018) 124–132.

[42] M. Faraji, N. Mohaghegh, A. Abedini, TiO_2 nanotubes/Ti plates modified by silver–benzene with enhanced photocatalytic antibacterial properties, New J. Chem. 42 (2018) 2058–2066.
[43] X. Yang, Y. Zhang, Y. Wang, C. Xin, P. Zhang, D. Liu, B.B. Mamba, K.K. Kefeni, A. T. Kuvarega, J. Gui, Hollow β-Bi_2O_3@CeO_2 heterostructure microsphere with controllable crystal phase for efficient photocatalysis, Chem. Eng. J. 387 (2020), 124100.
[44] Y. Sheng, Z. Wei, H. Miao, W. Yao, H. Li, Y. Zhu, Enhanced organic pollutant photodegradation via adsorption/photocatalysis synergy using a 3D g-C_3N_4/TiO_2 free-separation photocatalyst, Chem. Eng. J. 370 (2019) 287–294.
[45] N. Mohaghegh, M. Faraji, A. Abedini, Fabrication of electrochemically nonporous NiO–ZnO/TiO_2 nanotubes/Ti plates for photocatalytic disinfection of microbiological pollutants, J. Iran. Chem. Soc. 16 (2019) 1207–1215.
[46] N. Mohaghegh, M. Faraji, A. Abedini, Highly efficient multifunctional ag/TiO_2 nanotubes/Ti plate coated with MIL-88B(Fe) as a photocatalyst, adsorbent, and disinfectant in water treatment, Appl. Phys. A 125 (2018).
[47] Q. Wang, H. Li, X. Yu, Y. Jia, Y. Chang, S. Gao, Morphology regulated Bi_2WO_6 nanoparticles on TiO_2 nanotubes by solvothermal Sb^{3+} doping as effective photocatalysts for wastewater treatment, Electrochim. Acta 330 (2020), 135167.
[48] Z. Liu, Y. Song, Q. Wang, Y. Jia, X. Tan, X. Du, S. Gao, Solvothermal fabrication and construction of highly photoelectrocatalytic $TiO_{(2)}$ NTs/$Bi_{(2)}MoO_{(6)}$ heterojunction based on titanium mesh, J. Colloid Interface Sci. 556 (2019) 92–101.
[49] C. Xu, D. Li, X. Liu, R. Ma, N. Sakai, Y. Yang, S. Lin, J. Yang, H. Pan, J. Huang, T. Sasaki, Direct Z-scheme construction of g-C_3N_4 quantum dots/TiO_2 nanoflakes for efficient photocatalysis, Chem. Eng. J. 430 (2022), 132861.
[50] S. Zhou, N. Bao, Q. Zhang, X. Jie, Y. Jin, Engineering hierarchical porous oxygen-deficient TiO_2 fibers decorated with BiOCl nanosheets for efficient photocatalysis, Appl. Surf. Sci. 471 (2019) 96–107.